Observations of Electron Vorticity and Phase Space Holes in the Magnetopause Reconnection Separatrix

Narges Ahmadi[1], Stefan Eriksson[1], David Newman[2], Laila Andersson[1], Robert E. Ergun[1,3], Frederick D. Wilder[4]

[1]Laboratory for Atmospheric and Space Physics, University of Colorado, Boulder, Colorado, USA
[2]Department of Physics, University of Colorado Boulder, Boulder, CO,USA
[3]Department of Astrophysical and Planetary Sciences, University of Colorado, Boulder,Colorado, USA
[4]Department of Physics, University of Texas at Arlington, Arlington, USA.

Key Points:

- We observe enhanced electron vorticity at an earthward separatrix of magnetopause reconnection.
- The electron vorticity causes perturbations in the magnetic field.
- There is correlation between large amplitude phase space holes and enhanced vorticity in the dayside reconnection separatrix.

Corresponding author: Narges Ahmadi, `Narges.Ahmadi@lasp.colorado.edu`

Abstract

We report Magnetospheric MultiScale (MMS) observations of two electron vortices with a roughly 10 km or 2-3 electron skin depths cross-section across the magnetospheric separatrix of a dayside magnetopause reconnection. The enhanced electron vorticity, which is caused by a significant velocity shear in the electron flows streaming in opposite directions along northward-directed magnetic field lines, leads to perturbations perpendicular to the reconnecting magnetic field on the order of 1-2 nT. The high electron vorticity periods are also associated with electron phase space holes having the largest bipolar parallel electric field amplitudes $\sim$ 25 mV/m observed across this exhaust. Less intense $\sim$ 10 mV/m electron phase space holes propagate along a northward magnetic field away from the X-line within a northward reconnection exhaust. The electron phase space holes with the largest bipolar parallel electric fields are observed to propagate toward the X-line within discrete channels of southward and super-Alfvénic 1500 km/s electron flows in the magnetospheric separatrix layer.

1 Introduction

Magnetic reconnection is a physical process that converts magnetic energy into kinetic energy. This process happens throughout the universe where opposing magnetic field lines exist including at the Earth's magnetopause. The plasmas on the two sides of the Earth's dayside magnetopause current sheet are often characterized by a strong asymmetry of the magnetic field, plasma number density and temperature. The gradients of magnetic field and density are known to result in an Earthward displacement of the magnetosheath flow stagnation point relative to the magnetic reconnection X-line, where the in-plane reconnecting magnetic field changes direction. (Cassak & Shay, 2007, 2008) This is commonly referred to as asymmetric magnetic reconnection.(Pritchett & Mozer, 2009)

Previous numerical studies have predicted a rotation phenomenon for electrons in the exhaust region close to the separatrix of asymmetric magnetopause reconnection. Pritchett and Mozer (2009) used two-dimensional particle-in-cell (PIC) simulations of asymmetric reconnection in the presence of a moderate guide field ($\sim$ 50%) and showed a series of electron vortices form sunward of the magnetospheric separatrix region of a southward reconnection jet. Vorticity is the curl of the velocity vector and is a measure of local rotation of the fluid motion. In the simulation, these kinetic-scale electron vortices are proposed to be a result of the electron Kelvin-Helmholtz instability with a $\sim$0.3 d_i width (4 d_e with the ion to electron mass ratio of 200) and $\sim$1 d_i spacing between separate electron vorticity structures. Here, $d_i = c/\omega_{pi}$ is the ion inertial length and $\omega_{pi} = \sqrt{n_i e^2/m_i \epsilon_0}$ is the ion plasma frequency. The simulated electron vortices propagated at a speed of about $0.3 v_A$ with $v_A = B/\sqrt{\mu_0 n_i m_i}$ being a local ion Alfvén speed and they were associated with fluctuating dissipation regions and changes in the guide magnetic field magnitude that may impact the reconnection topology and energy dissipation. Fermo et al. (2012) used PIC codes to suggest that electron Kelvin-Helmholtz vorticity formation near the separatrix can fold the magnetic field lines and may seed secondary islands.

Observations of electron scale vortices was not feasible before the Magnetospheric MultiScale (MMS) mission due to limited time resolution plasma measurements.(Burch et al., 2016) Phan et al. (2016) showed enhanced electron vorticity observed within the reconnection exhaust region and the exhaust boundaries downstream of the X-line using MMS data. Observed reductions in electron vorticity magnitude toward the inflow region indicated that the enhancements in vorticity resulted from the reconnection processes. In a recent study, Hwang et al. (2019) showed that the electron vorticity can cause magnetic field fluctuations along the reconnecting magnetic field component near the electron diffusion region (EDR) in the magnetotail and they proposed that it could be a signature of spatial proximity to an EDR. They also found that the magnitude of the electron vorticity increases toward the edge of the electron jet due to a flow shear of the out-of-plane electron velocity. Consequently, it is possible for the electron vorticity to cause fluctuations in the local magnetic field changing the topology, and therefore potentially impacting the local small-scale physics of magnetic reconnection. Ergun et al. (2019) proposed a model of electromagnetic drift waves propagating along the current sheet in the vicinity of a subsolar magnetopause EDR region. They show how these drift waves can also be represented as a series of electron vortices superimposed on a primary electron drift motion along the current sheet in a direction parallel to the X-line. The drift waves displace or corrugate the current sheet, which may also potentially displace the EDR.

Another important feature often associated with magnetic reconnection is the presence of electrostatic solitary waves (ESWs). Graham et al. (2016) explored Cluster satellite observations of ESWs, consisting of solitary bipolar variations of the parallel electric field in the vicinity of asymmetric reconnection exhausts at the dayside magnetopause. Due to the spin-plane limitation of the Cluster electric field instrument, without a dedicated electric field measurement along the spin axis, that ESW study was limited to very short time periods when burst mode electric field data were available in a fortuitous configuration relative to the magnetic field. Matsumoto et al. (2003) also reported a fortuitous ESW encounter from Geotail satellite observations at the Earthward boundary of an asymmetric dayside magnetopause exhaust. The Geotail mission, as with the Cluster and THEMIS missions, suffers from the absence of a high-quality axial electric field measurement, with limited parallel electric field measurements to address the question of where ESWs occur relative to reconnection exhaust and separatrix regions, and whether the ESWs correspond to electron phase space holes. However, the MMS mission, with its complete set of electric field vector observations, is able to resolve small-scale exhaust structure and address the instabilities that generate ESWs to determine their impact on asymmetric reconnection. ESWs have the potential to be very important in asymmetric reconnection, since they may be able to dissipate strong currents and couple different electron populations, as suggested by Graham et al. (2016). Past observations and numerical simulations suggest that ESWs develop in the separatrix regions of magnetic reconnection exhausts.(Drake et al., 2003; Cattell et al., 2003; Fujimoto & Machida, 2006; Goldman et al., 2008; Graham et al., 2015) It has also been suggested that ESWs form near the EDR due to bi-streaming electron populations (Goldman et al., 2008; Swisdak et al., 2018), and they could potentially access the asymmetric exhaust, since the X-line is separated from the inflow stagnation point. Huang et al. (2014) explored PIC simulations of anti-parallel reconnection to suggest that electron phase space holes can form within the density cavity of the separatrix regions due to a two-stream electron beam instability between electrons flowing toward and away from the X-line. Goldman *et al.* (2014) employed a symmetric PIC simulation for weak guide magnetic field conditions to suggest that electron phase space holes may form along all four separatrix regions. Lapenta et al. (2011) performed PIC simulations of symmetric magnetic reconnection with different guide field strengths and they showed that a strong electron flow develops along the separatrices in all cases, which is sufficient to lead to the onset of streaming instabilities and to form bipolar parallel electric field signatures. They also showed that the predominant strength of the inward flow along one pair of separatrices tends to increase the prevalence of bipolar signatures along those flow channels without suppressing them altogether along the other two separatrices. Asymmetric reconnection simulations reported by Cazzola et al. (2015) (e.g., Fig. 14) and by Chang et al. (2021) (e.g.,

Fig. 8) also confirm the formation of bipolar fields (electron phase space holes) along the magnetosphere-side separatrix.

In this paper, we investigate a possible relation between electron vorticity and electron phase space holes in a case of asymmetric magnetopause reconnection as recorded by the four MMS satellites in a high-quality tetrahedron formation near the subsolar region. In this set of observations, a large magnitude of the obtained electron vorticity coincides with the largest phase space hole magnitudes present along the earthward-side, magnetospheric separatrix of a northward exhaust. In section 2, we present an overview of the subsolar exhaust as observed by MMS to the north of a dayside magnetopause X-line and the signatures which are consistent with a magnetospheric separatrix earthward of a northward reconnection exhaust. In section 3, we explore the size and the speed of the electron vorticity structures using a timing analysis method of the four satellite observations and we compare and contrast the observations with reported PIC simulation predictions. In section 4, we show that large amplitude phase space holes are present in the regions of vorticity enhancements and discuss their size and speed. Section 5 includes a summary and conclusion of this study into kinetic-scale separatrix structures.

2 MMS Event Overview

The four MMS satellites have repeatedly crossed the magnetopause boundary to capture the dynamics of dayside asymmetric magnetic reconnection.(Burch et al., 2015) The MMS satellites carry identical instruments capable of gathering high time resolution particle and fields data while operating in burst mode.(Baker et al., 2016; Ergun et al., 2016; Kawa & Lin, 2016; Contel et al., 2016; Lindqvist et al., 2016; Pollock et al., 2016; Russell et al., 2016; Torbert et al., 2016)

The MMS satellites traversed the magnetopause from the magnetosheath into the magnetosphere at ∼10:09:45 UT on 29 January 2017. The four satellites were in a tetrahedron formation at this time with a separation distance of ∼7km at [10.2, -2.9, 1.8] R_E in GSM coordinates. Figure 1 shows an overview of the crossing as recorded by the MMS1 satellite with all instruments operating in a burst mode. Panels a and b show ion and electron energy fluxes measured by the fast plasma investigation (FPI) instrument in 150 ms cadence for ions and 30 ms cadence for electrons. The third and fourth panels (c and d), respectively, show the three components of the magnetic field and the electric field

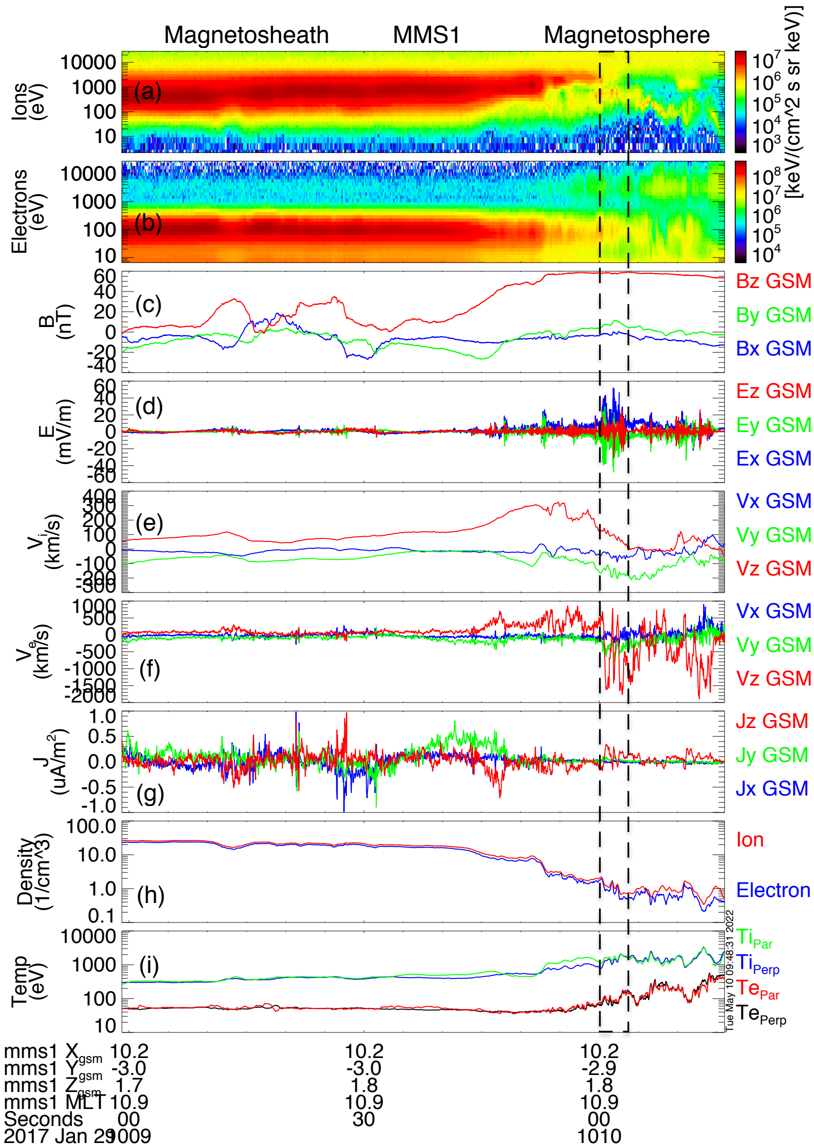

Figure 1. Overview of the magnetopause crossing using MMS1 data. (a) Ion energy flux (b) Electron energy flux (c) Magnetic field vector (d) Electric field (e) Ion velocity (f) Electron velocity (g) Current density from FPI instrument (h) Ion (red line) and electron density (blue line) (i) Ion and electron temperatures perpendicular and parallel to the background magnetic field.

in the GSM coordinate system. The magnetic field data are measured by the Fluxgate Magnetometer (FGM) instrument with 128 samples/second and electric field data are provided by the Electric field Double Probes (EDP) instruments with 8192 samples/second. Panels e and f show the three components of the ion and electron velocities in the GSM coordinate system as measured by the FPI instruments. The current density calculated using FPI instrument is shown in panel g. The ion and electron densities, and the temperatures perpendicular and parallel to the magnetic field, are displayed in panels h and i. The plasma densities decreased and the temperatures increased as the satellites moved from the magnetosheath into the magnetosphere as expected across the magnetopause.

At about 10:09:44 UT, the V_{iZ} component of the ion flow begins to increase toward a maximum value close to 300 km/s in a northward Z direction, at nearly the same time as the Z component of the magnetic field increases toward a maximum of about 60 nT. This $V_{iZ} \sim 300$ km/s jet speed roughly corresponds to half of the ion Alfvén speed ($v_A \sim$ 585 km/s), which is calculated from the average of B_Z and the average ion density in the interval of an increasing ion flow. This time period reflects an MMS crossing of a northward magnetic reconnection jet on the earthward side of the dayside magnetopause in agreement with a positive V_{iZ} and a positive B_Z.

A measured ∼600 km/s electron flow, which is almost equal the estimated Alfvén speed, is also recorded in the same northward direction as the ion exhaust. As the ion flow starts to decrease, we observe several enhancements of the sunward X component of the electric field, with some periods showing E_X above ∼40 mV/m. This positive electric field, which is aligned with the magnetopause normal direction, is consistent with the expectations of a separatrix layer on the earthward side of an actively reconnecting magnetopause current sheet.(Swisdak et al., 2018) This approximately normal electric field acts to decelerate the ion inflow from the magnetosheath and it ensures an overall charge neutrality with the much less dense population of magnetospheric electrons. A comparison of the measured components of the electric field with the components of the $V_e \times B$ electric field (not shown) suggests that the electrons are frozen-in to the magnetic field. In this same region of enhanced sunward E_X, we also observe significant reversals in V_{eZ} from northward ∼600 km/s flows in the reconnection exhaust to southward flows toward the X line with amplitudes as large as 2000 km/s. These high velocity electron flows are associated with an electron population with energies below 1000 eV.

MMS also observed large amplitude parallel electric field fluctuations in this region that consists of several V_{eZ} reversals. The presence of multiple channels of fast ∼1500 km/s southward flows suggests that the MMS1 satellite may have traversed a system of filamentary currents at the exhaust boundary in the magnetospheric separatrix region.

3 Observation of Electron Vorticity

We calculate electron vorticity or $\nabla \times V_e$ from the measurements of electron velocity and position information at the four MMS satellite. Figure 2 shows a subset of electron and magnetic field measurements from all four MMS satellites in the 4 s region of interest from 10:10:00 UT to 10:10:04 UT when the large-amplitude electric field structures and high-speed electron flow reversals are observed near the Earthward boundary of the reconnection exhaust. A box outlined by the dashed lines in Figure 1 marks this 4 s region of interest. All vector components are shown in a boundary normal LMN coordinate system that we obtained as follows. We first find a large-scale boundary normal coordinate system of the magnetopause current sheet in GSM coordinates with L_0=[-0.047, 0.318, 0.947], M_0 = [-0.241, -0.923, 0.298] and N_0 = [0.969, -0.214, 0.120]. Here, N_0 is the direction of the cross-product normal for the average external magnetic fields at 10:08:52.700 UT and 10:10:05.300 UT, M_0 is the normalized cross-product of N_0 with the direction of maximum variance of the magnetic field for this same time period, and $L_0 = M_0 \times N_0$. However, the normal component of the magnetic field of this LMN system is found to point in a positive direction across the northward exhaust region. This is inconsistent with a reconnection X line to the south of the MMS satellites, which is expected to connect a northward magnetospheric field with an Earthward directed normal component across the magnetopause layer to the adjacent magnetic field of the magnetosheath. The large-scale LMN system, therefore, needs a slight correction that we achieve on the basis of a multi-satellite timing analysis of the V_{eZ} GSM component for a sharp southward flow reversal that MMS1 observed to be centered at 10:10:01.800 UT in the magnetospheric separatrix layer. Taking MMS1 as the reference satellite, and shifting the 30 ms cadence V_{eZ} observations forward in time by 41 ms for MMS2, 74 ms for MMS3 and 29 ms for MMS4, we obtain a timing analysis boundary normal vector of the V_{eZ} signal between the four MMS satellites. This unit vector is used to define a revised L = [-0.040, -0.227, 0.973] due to its alignment with a Z_{GSM} direction. We find a corrected normal direction N = [0.966, -0.259, -0.020] as the normalized cross-product of this L with M_0, while M = [-0.256, -0.939, -0.230], completes the orthogonal system as the cross-product of N and L. This LMN system is now optimized for a local analysis of the observed electron flow reversals of the magnetospheric separatrix from a small 8.5 degrees rotation of the normal vector. This correction of the direction of the normal vector also results in a negative B_N component of the magnetic field as expected across a northward reconnection exhaust region near the subsolar magnetopause.

Figure 2a displays a subset of measurements at all four MMS satellites with panels 1 and 2 showing the L and M components of the electron velocity, panels 3 and 4 showing the M and N components of the magnetic field, and panel 5 showing the electron density. Panel 6 presents the derived electron vorticity in LMN coordinates or $\nabla \times V_e$, which is obtained from the measurements of electron velocity and position information at the four MMS satellites. The vorticity corresponds to a rotation or a shear in the velocity field. Figure 2b displays the MMS satellite separations with a high tetrahedron quality factor (TQF=0.909) of the formation at 10:10:02 UT when MMS recorded the high-speed electron flow reversals and the corresponding electron vorticity displayed in Figure 2a. Figure 2c depicts a schematic of the asymmetric reconnection exhaust region with a red line showing the inferred, and highly localized, MMS path across the magnetospheric separatrix on the basis of a multi-satellite timing analysis of a sharp southward V_{eZ} flow reversal at 2017-01-29/10:10:01.800 UT.

The electron vorticity vector is clearly enhanced in the region of electron flow reversals at 10:10:01.5-10:10:03 UT. It is predominantly aligned with a positive M-direction and to a lesser extent with a negative N-direction as indicated between the two red dashed, vertical lines. In other words, it is perpendicular to the background mostly northward ($B_L > 0$) magnetic field. The large vorticity region coincides with changes in the B_M (guide field) and the B_N components of the magnetic field as also illustrated in panels 3 and 4. The B_M component of the magnetic field (the reconnection guide field) is about -18 nT which is about 30% of the B_L or reconnecting magnetic field. The high shear in the L direction of the electron velocity drives the electron vorticity in the M and N directions.

In order to appreciate the connection between the electron flow reversals and the deduced electron vorticity, we display the V_e vector field components of the NL-plane as measured along the MMS1 and MMS3 satellite trajectories in Figure 3. Here, the tem-

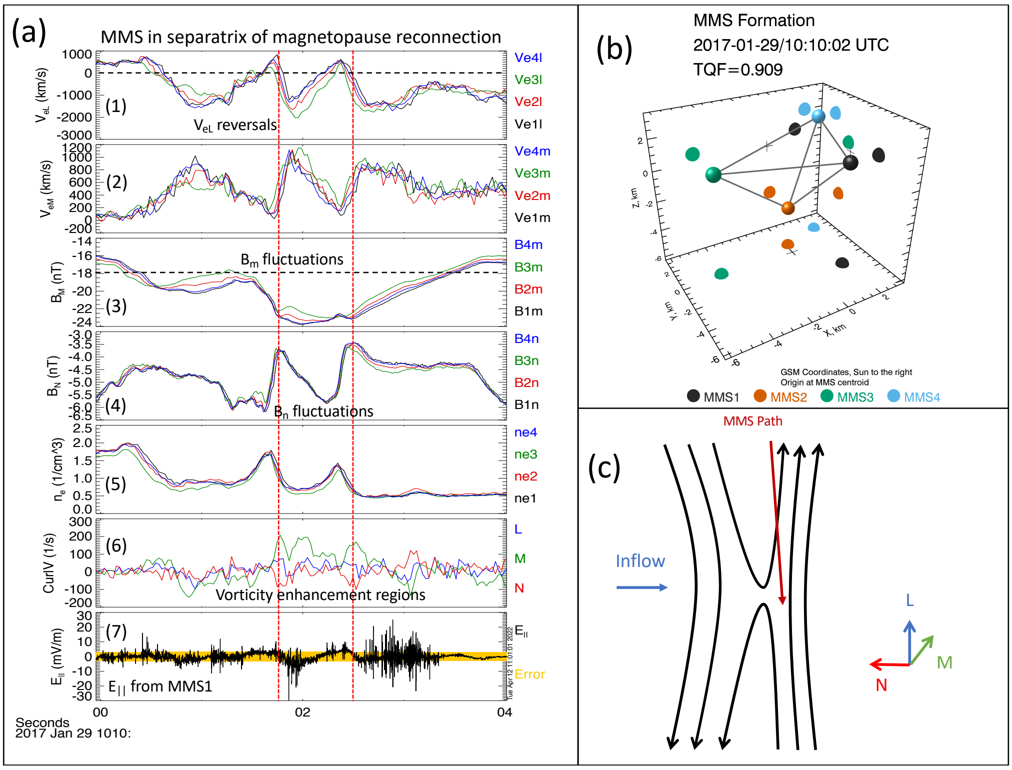

Figure 2. (a) Region of interest at 10:10:00-10:10:04 UT with a large electron vorticity associated with the magnetospheric separatrix region of dayside magnetopause reconnection. (1) L component of electron velocity (V_{eL}), (2) V_eM component, (3) B_M component of magnetic field, (4) B_N component of the magnetic field, (5) electron density for all four satellites, (6) multi-satellite electron vorticity calculation in LMN coordinates, and (7) parallel electric field from MMS1, (b) MMS formation at the 10:10:02 UT time of crossing, and (c) the sketch of MMS path across the local section of the magnetospheric separatrix layer. The two red vertical dashed lines at 10:10:01.680 UT and 10:10:02.490 UT mark the V_{eL} flow reversal of two electron vorticity structures.

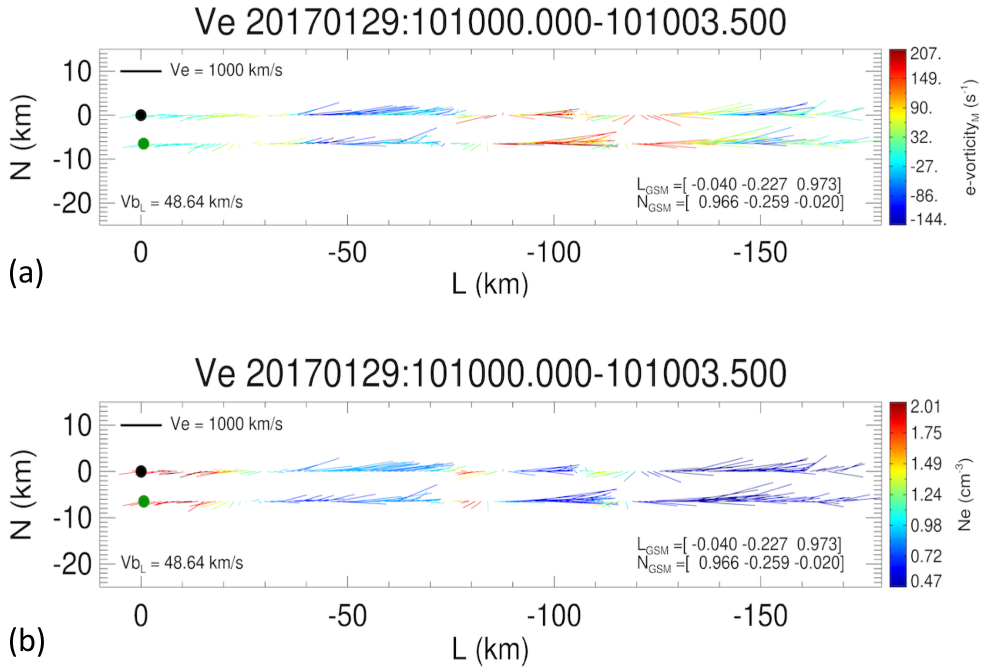

Figure 3. Vector analysis of electron velocity for MMS1 and MMS3. (a) The electron velocity vectors are displayed in the NL-plane with the M component of electron vorticity shown in color, (b) electron velocity shown in the NL-plane with color showing the measured electron density. We identify the center of two V_e rotations corresponding to the two strong electron vorticity events with the first rotation (vorticity) centered at $L \sim -85$ km for MMS3 and $L \sim -90$ km for MMS1, and the second rotation centered at $L \sim -115$ km for MMS3 and $L \sim -120$ km for MMS1.

poral information as recorded by the two satellites for a 3.5 s period from 10:10:00 UT are converted to spatial L-distances using the northward-pointing L-vector of the timing method and the corresponding boundary speed $v_L \approx 48.6$ km/s by which the electron velocity field and the associated electron vorticity structures are observed to propagate in a northward L-direction away from the X line. The northward electron vorticity propagation is reflected, therefore, in a southward or -L MMS trajectory direction of this figure. The origin at $(N, L) = (0, 0)$ is taken as the location of MMS1 (black dot) at 10:10:00 UT with the location of MMS3 (green dot) shown with its NL-plane separation, ΔL=-0.64 km and ΔN=-6.47 km, from MMS1 at this same time. The MMS2 and MMS4 satellite trajectories are excluded here due to their close N-separation from MMS1, with MMS2 at ΔN=-2.43 km and MMS4 at ΔN=-0.62 km, such that their V_e vectors would directly overlap with the vector field at MMS1. The figure shows how the electron velocity V_e vectors are changing direction and amplitude as the two MMS satellites fly through this separatrix region. In panel a, the color represents the out-of-plane M-component of the electron vorticity and in panel b, color displays the observed electron density along the two MMS trajectories.

Based on the V_e vector plots of Figure 3, we identify the center of two counter-clockwise V_e rotations coincident with the two strongest electron vorticity events. The center of one vorticity enhancement is present at $L \sim -85$ km for MMS3 and $L \sim -90$ km for MMS1, and a second vorticity structure is centered near $L \sim -115$ km at MMS3 and $L \sim -120$ km at MMS1. The electron velocity field of Figure 3 illustrates how the original V_e measurements are reproduced in the deduced electron vorticity. A comparison of the two panels of Figure 3 also suggests a presence of two density enhancement features (see panel b) just ahead of the northward-propagating vorticity structures at $|L| =$ 80 km and $|L| = 110$ km. These density enhancements indicates that the MMS satellites are entering the exhaust region as the magnetopause boundary oscillates.

The two electron vorticity structures are kinetic-scale with Figure 3 suggesting an approximate 10-20 km cross-section. This dimension corresponds to $2-4$ d_e where $d_e \sim$ 5 km is an electron inertial length for the average 1.1 cm^{-3} plasma density recorded at this time (see Figure 2a, panel 5). Given that $d_i = (m_p/m_e)^{1/2} d_e$, the electron vortices are only about $0.05 - 0.09$ d_i in terms of the local ion inertial length. They are moving away from the X-line and along the northward-directed reconnecting magnetic field lines with a 48.6 km/s propagation speed or $v_L \sim 0.1 v_A$. These particular electron vorticity structures that MMS observed at the magnetospheric separatrix layer are somewhat smaller in size and their propagation speed is somewhat slower as compared with the typical $\sim 0.3d_i$ size electron vortices that Pritchett and Mozer (2009) simulated to move at about $\sim 0.3v_A$ in a 2D PIC code.

The counter-clockwise rotation of the electron velocity present in the NL-plane of Figure 3 corresponds to a clockwise loop of current that induces a magnetic field deflection in a negative M direction. This localized electron vorticity is the likely origin of the highly localized and rather weak 2 nT magnitude increases of the measured guide magnetic field, which are shown to be centered at the times of each of the two red, dashed vertical lines of Figure 2a (see panel 3) that mark the locations of the two V_{eL} flow reversals of each electron vorticity structure. The two electron vorticity structures are not perfectly contained in the NL-plane with a single M-component of the vorticity vector as indicated by the presence of an additional N-component of the vorticity vector in panel 6 of Figure 2a. This finite N-component of the electron vorticity vector is reflected in the enhanced $V_{eM} > 0$ velocity changes, which are centered at the same times as the two red, dashed vertical lines (see Figure 2a, panel 2) of the V_{eL} reversals. These $V_{eM} > 0$ velocity changes induce a magnetic field fluctuation in the positive N-direction as reflected by the observed ∼2 nT magnitude decreases of the B_N component of the magnetic field (see Figure 2a, panel 4), which are co-located with the V_{eL} reversals of the electron vorticity. The guide magnetic field B_M also displays a large-scale ∼6 nT change in a negative M-direction over a 1.5 s duration period from ∼10:10:01.5 UT to ∼10:10:03 UT. This change of the guide-field, albeit coincident with the region of enhanced electron vorticity, is more likely supported by a larger-scale current system along the L-direction that may consist of the $V_{eL} > 0$ before 10:10:00.5 UT and the sustained $V_{eL} < 0$ after 10:10:03 UT.

4 Electron Phase Space Holes

The observations of large electron vorticity across the magnetospheric separatrix region coincide with a presence of large amplitude bipolar parallel electric field structures, which are also known ESWs. (Graham et al., 2016; Matsumoto et al., 2003) These bipolar structures are associated with amplitudes as high as 25 mV/m in this dayside event and they signal the presence of electron phase space holes. An electron phase space hole is equivalent to a very localized region of surplus positive charge and a diverging electric field. An electron phase space hole moving along the background magnetic field will therefore generate a short-duration bipolar signal of the parallel electric field ($E_{\|}$). Figure 4 displays the instances of a large number of highly localized bipolar $E_{\|}$ ESW structures as primarily recorded by the axial double-probes of the EDP instrument at 8192 Hz on all four MMS satellites across the northward reconnection exhaust region and the adjacent vorticity region of the magnetospheric separatrix. In panels d to g, the instances of bipolar ESWs are color-coded at each satellite with a red plus symbol corresponding to a positive-then-negative bipolar $E_{\|}$ and each black plus symbol likewise indicating a negative-then-positive bipolar $E_{\|}$. The red ESWs likely represent fast electron phase space holes moving *parallel* with the magnetic field, while the black ESWs represent electron phase space holes moving in the *anti-parallel* magnetic field direction. The magnetic field does not change direction inside the vorticity region of interest, where it is predominantly directed in a northward L direction as shown in panel a. This means that the assumed electron phase space holes are propagating in opposite directions of the magnetospheric separatrix region. In comparing the propagation direction of electron phase space holes and the direction of the electron velocity, it is clear that the electron holes are streaming in the same direction as the electron flows, whether along the northward $V_{eL} \sim 600$ km/s exhaust and away from the X-line before MMS encountered the separatrix region, or in a southward direction of the fast $V_{eL} \sim 1,500$km/s flow channels that we associate with regions of enhanced electron vorticity structures.

Established techniques for directly determining the velocity of the electron phase space holes in this time interval cannot be used. The holes are too slow to estimate their velocity from magnetic field perturbations (Andersson et al., 2009) and they are too fast to estimate a propagation velocity from a timing difference between the potential measured on two opposite electric field probes. The later limitation is particularly stringent because $\mathbf{B}$ is primarily directed along Z_{GSM} and the associated ~1 ms duration of the ESWs is too short to resolve a time delay of the corresponding potential signature for the relatively short 29.2 m separation between the two opposite axial probes.

We can nevertheless make a rough estimate of the electron phase space hole velocity as follows: The temporal separation of the largest (negative-to-positive) bipolar $E_{\|}$ field peaks during this period are ~ 0.25ms (e.g., Fig. 5b). Given a Debye length of $\lambda_e \sim 100$m based on the density of $\sim 0.5cm^{-3}$ and a parallel electron temperature of ~ 100eV representative of the times when the largest bipolar fields are observed, an electron phase

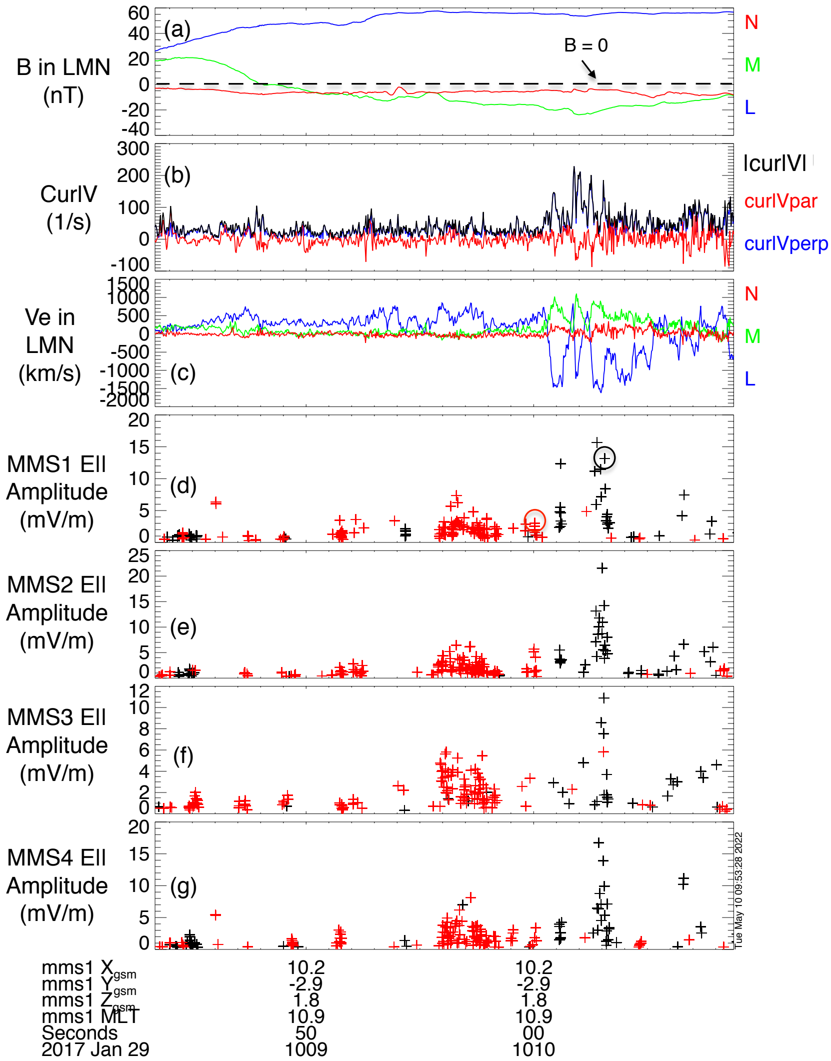

Figure 4. : Instances of observed phase space holes on all four MMS satellites. (a) Magnetic field, (b) Electron vorticity shown perpendicular (blue line), parallel (red line) to magnetic field and total (black line), (c) Electron velocity, (d) Phase space holes on MMS1, (e) Phase space holes on MMS2, (f) Phase space holes on MMS3 and (g) Phase space holes on MMS4. On panel d, marked phase space holes in circles are shown in figure 5.

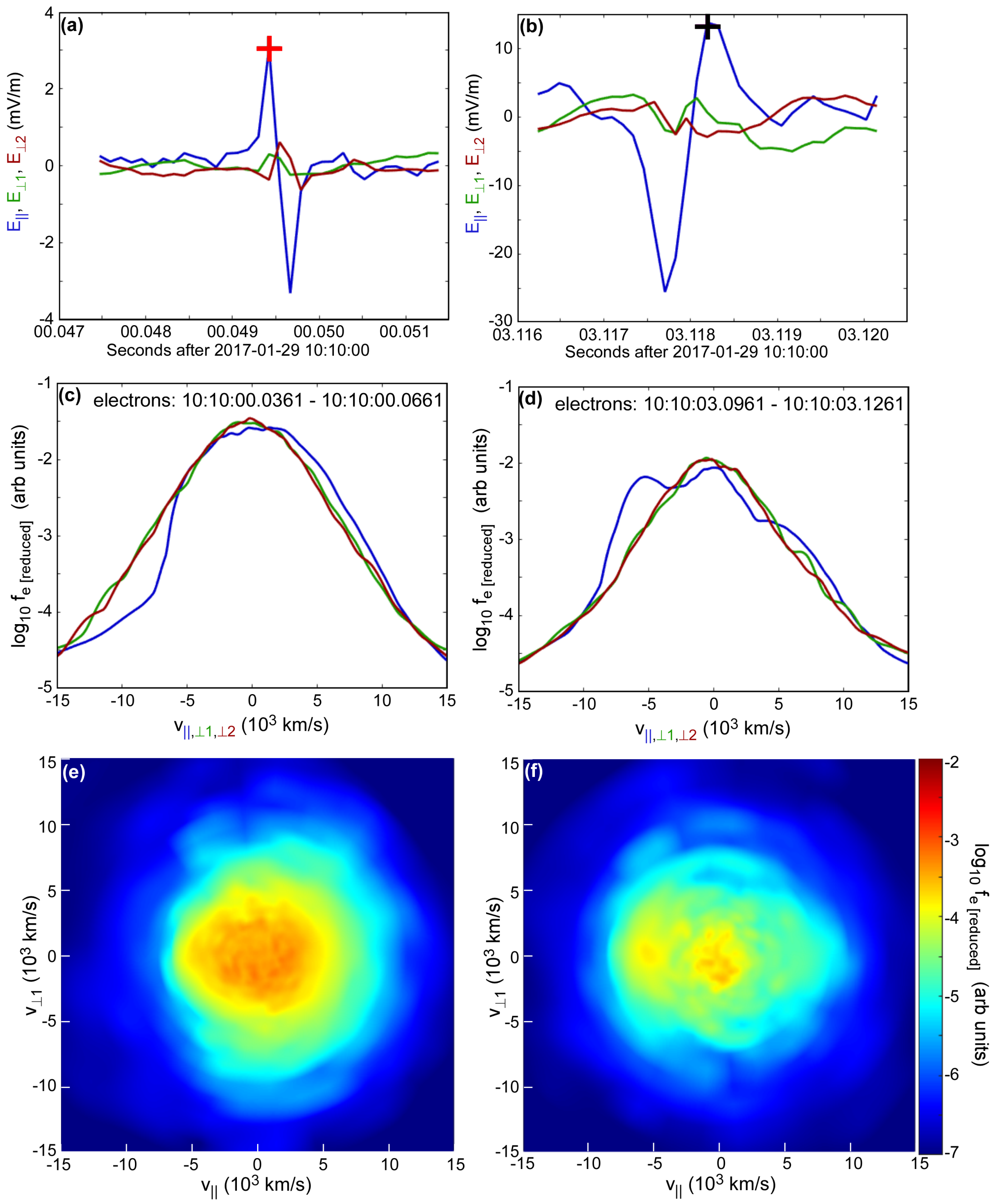

Figure 5. Panels (a) and (b) Electric field components in field-aligned coordinates for two bipolar $E_{\|}$ events from MMS1 of opposite polarity (as indicated in panel d of Fig. 4). Each interval plotted covers ± 2 ms on either side of the detection time, which is marked by the respective red and black '+' signs. Panels (c) and (d) Reduced electron distributions along the three orthogonal field-aligned directions for the 30 ms FPI measurement interval containing the respective bipolar EH events in panels (a) and (b). (e) and (f) electron distributions in $v_{\|} - v_{\perp}$ plane at the interval of the EH events.

space hole with a typical spatial width of $\sim$ 2–10λ_e would have a velocity in the -**B** direction of ∼800–4000 km/s.(Andersson et al., 2009; Hutchinson, 2017; Holmes et al., 2018) Such a velocity is consistent with the valley in the reduced parallel distribution in Fig. 5d. The weaker positive-to-negative bipolar $E_{\parallel}$ in Fig. 5a is associated with a broad plateau in the simultaneous reduced distribution (Fig. 5c) in the $+v_{\parallel}$ direction, with no distinct valley. This is typical of times when weak bipolar fields of either polarity are observed during the time interval in figure 4. Note that the 30ms interval covered by each FPI distribution can contain multiple electron phase space holes—each of which has a duration of 1ms—and so the interpretation is complicated by temporal averaging. Figures 5e and 5f show 2D electron distributions in the $v_{\parallel}-v_{\perp}$ plane for the interval of the electron hole events. The left distribution (Fig. 5e) is characterized by a broad plateau surround by a hotter population. This distribution is shifted toward positive $v_{\parallel}$. However, there are no features that can be easily correlated with the observed bipolar field. The right distribution (Fig. 5f), on the other hand, appears to consist of a beam moving in the -$v_{\parallel}$ direction that is clearly separated from the core population. The beam-like component may be associated with a beam-plasma instability that saturates by producing electron holes. However, a beam-like feature can also result from passing electrons being accelerated by the positive potential of an electron hole as it crosses the region. Since electron holes pass the detector over times short compared to the 30 ms interval measured by FPI, the observed distribution is likely a mixture of an unmodified component and a component temporarily modified by the presence of electron holes.

5 Summary and Conclusions

In this study, we presented observations of electron vorticity across the magnetospheric separatrix region of dayside magnetopause reconnection as recorded by the MMS satellites and their relation with electron phase space holes. The enhanced electron vorticity is directly associated with a region of high-speed electron flow reversals between ∼600 km/s northward exhaust flows and several bursts of ∼1,500 km/s southward electron flows as identified in the data. The electron vorticity, which is dominant in the directions perpendicular to the reconnecting (L component) magnetic field, and the associated current loops induces a ∼2 nT magnetic field perturbation of both the guide magnetic field along the out-of-plane $-M$-direction and the normal component of the magnetic field. The positive M-component of the electron vorticity vector, therefore, enhances the local magnitude of a negative guide field and the negative N-component of the vorticity vector reduces the magnitude of a negative normal magnetic field. Using a multi-satellite timing analysis of the V_{eZ} component of the electron velocity, we find that the vorticity structures are moving away from the X line along the northward L direction of the reconnecting magnetic field at $v_L \approx 49$ km/s or $v_L \sim 0.1v_A$. The estimated ∼10-20 km size of two vorticity structures corresponds to a kinetic-scale dimension of $2-4d_e$ or $0.05-0.09d_i$. These electron vorticity structures are roughly three times as small in size and propagation speed as compared with similar predictions of electron vorticity structures from a 2D PIC numerical simulation by Pritchett and Mozer (2009) for a similar strength of a guide field. In comparison, Ergun et al. (2019) modeled a series of electron vorticity structures propagating along the current sheet in the vicinity of a subsolar magnetopause EDR region in a direction parallel to the X line or along the M direction, while our observations of the electron vorticity structures in the separatrix of magnetopause reconnection indicates they are propagating in the L direction or along the reconnecting magnetic field.

The MMS satellites recorded large-amplitude electron phase space holes in the region of electron vorticity structures at the exhaust boundary with the magnetospheric-side separatrix. The velocity shear of two counter-streaming electron beams that generated this kinetic-scale electron vorticity likely also supported the formation of these electron phase space holes. MMS observed a northward propagation of moderate strength ∼10 mV/m electron phase space holes along the ∼600 km/s northward exhaust flow region away from the X line. More intense ∼25 mV/m phase space holes were subsequently observed to propagate toward the X-line and mostly within channels of fast ∼1,500 km/s southward electron flows associated with the magnetospheric separatrix layer. Using reduced parallel distributions of electrons, we showed that a typical electron phase space hole with a spatial width of $\sim$ 2–10λ_e in a general agreement with the observed electron density and electron temperature would have a velocity in the -**B** direction of ∼800–4000 km/s. Based on the PIC simulations performed by Cazzola et al. (2015) and Chang et al. (2021), phase space holes are dominant on magnetospheric side of reconnection separatrix in asymmetric magnetic reconnection in agreement with these MMS observations.

Acknowledgments

This work was funded by the NASA MMS Guest Investigator project Grant 80NSSC18K1382. The authors recognize the tremendous effort in developing and operating the MMS satellites and instruments and sincerely thank all involved. MMS satellite measurements are publicly available via the MMS Science Data Center (https://lasp.colorado.edu/mms/sdc/public/).

References

Andersson, L., Ergun, R. E., Tao, J., Roux, A., LeContel, O., & et. al. (2009). New features of electron phase space holes observed by the themis mission. *Physical Review Letters*, *102*, 225004. (DOI:10.1103/PhysRevLett.102.225004)

Baker, D. N., Riesberg, L., Pankratz, C. K., Panneton, R. S., Giles, B. L., Wilder, F. D., & Ergun, R. E. (2016). Magnetospheric multiscale instrument suite operations and data system. *Space Sci. Rev.*, *199*, 545–575. (DOI:10.1007/s11214-014-0128-5)

Burch, J. L., Moore, T. E., Torbert, R. B., & Giles, B. L. (2015). Magnetospheric multiscale overview and science objectives. *Space Sci. Rev.*, *199*, 5-21. (DOI:10.1007/s11214-015-0164-9)

Burch, J. L., Moore, T. E., Torbert, R. B., & Giles, B. L. (2016). Magnetospheric multiscale overview and science objectives. *Space Sci. Rev.*. (DOI:10.1007/s11214-015 -0164-9)

Cassak, P. A., & Shay, M. A. (2007). Scaling of asymmetric magnetic reconnection: General theory and collisional simulations. *Phys. Plasmas*, *14*, 102114. (DOI:10.1063/1.2795630)

Cassak, P. A., & Shay, M. A. (2008). Scaling of asymmetric hall magnetic reconnection. *Geophys. Res. Lett*, *35*, L19102. (DOI:10.1029/2008GL035268)

Cattell, C., Dombeck, J., Wygant, J., Drake, J. F., Swisdak, M., Goldstein, M. L., … Balogh, A. (2003). Cluster observations of electron holes in association with magnetotail reconnection and comparison to simulations. *J. Geophys. Res.*, *110*, A01211. (DOI:10.1029/2004JA010519)

Cazzola, E., Innocenti, M. E., Markidis, S., Goldman, M. V., Newman, D. L., & Lapenta, G. (2015). On the electron dynamics during island coalescence in asymmetric magnetic reconnection. *Physics of Plasmas*, *22*, 092901. (DOI:10.1063/1.4929847)

Chang, C., Huang, K., Lu, Q., Sang, L., Lu, S., Wang, R., & et al. (2021). Particle-in-cell simulations of electrostatic solitary waves in asymmetric magnetic reconnection. *J. Geophys. Res.*, *126*, e2021JA029290. (DOI:10.1029/2021JA029290)

Contel, O. L., Leroy, P., & et al. (2016). The search-coil magnetometer for mms. *Space Sci. Rev.*, *199*, 257–282. (DOI:10.1007/s11214-014-0096-9)

Drake, J. F., Swisdak, M., Cattell, C., Shay, M. A., Rogers, B. N., & Zeiler, A. (2003). Formation of electron holes and particle energization during magnetic reconnection. *Science*, *299*, 873.

Ergun, R. E., Hoilijoki, S., Ahmadi, N., Schwartz, S. J., Drake, F. D. W. J. F., & et al. (2019). Magnetic reconnection in three dimensions: Modeling and analysis of electromagnetic drift waves in the adjacent current sheet. *J. Geophys. Res*, *124*, 10,085–10,103. (DOI:10.1029/2019JA027275)

Ergun, R. E., Tucker, S., Westfall, J., Goodrich, K. A., Malaspina, D. M., Summers, D., & et al. (2016). The axial double probe and fields signal processing for the mms mission. *Space Sci. Rev.*, *199*, 167–188. (DOI:10.1007/s11214-014-0115-x)

Fermo, R. L., Drake, J. F., & Swisdak, M. (2012). Secondary magnetic islands generated by the kelvin-helmholtz instability in a reconnecting current sheet. *Physical Review Letters*, *108*, 255005. (DOI:10.1103/PhysRevLett.108.255005)

Fujimoto, K., & Machida, S. (2006). A generation mechanism of electrostatic waves and subsequent electron heating in the plasma sheet-lobe boundary region during magnetic reconnection. *J. Geophys. Res.*, *111*, A09216. (DOI:10.1029/2005JA011542)

Goldman, M. V., Newman, D. L., & Pritchett, P. (2008). Vlasov simulations of electron holes driven by particle distributions for pic reconnection simulations with a guide field. *Geophys. Res. Lett.*, *35*, L22109. (DOI:10.1029/2008GL035608)

Graham, D. B., Khotyaintsev, Y. V., Vaivads, A., & Andre, M. (2015). Electrostatic solitary waves with distinct speeds associated with asymmetric reconnection. *Geophys. Res. Lett.*, *42*, 215-224. (DOI:10.1002/2014GL062538)

Graham, D. B., Khotyaintsev, Y. V., Vaivads, A., & Andre, M. (2016). Electrostatic solitary waves and electrostatic waves at the magnetopause. *J. Geophys. Res.*, *121*, 3069-3092. (DOI:10.1002/2015JA021527)

Holmes, J. C., Ergun, R. E., Newman, D. L., Ahmadi, N., & et. al. (2018). Electron phase space holes in three dimensions multispacecraft observations by magnetospheric multiscale. *Journal of Geophysical Research*, *123*, 9963-9978. (DOI:10.10292/2018JA025750)

Huang, C., Lu, Q., Wang, P., Wu, M., & Wang, S. (2014). Characteristics of electron holes generated in the separatrix region during antiparallel magnetic reconnection. *J. Geophys. Res.*, *119*, 6445-6454. (DOI:10.1002/2014JA019991)

Hutchinson, I. (2017). Electron holes in phase space: What they are and why they matter. *Physics of Plasmas*, *24*, 055601. (DOI:10.1063/1.4976854)

Hwang, K., Choi, E., Dokgo, K., Burch, J. L., Sibeck, D. G., Giles, B. L., & et al. (2019). Electron vorticity indicative of the electron diffusion region of magnetic reconnection. *Geophysical Research Letters*, *46*, 6287–6296. (DOI:10.1029/2019GL082710)

Kawa, S. R., & Lin, S.-J. (2016). Magnetospheric multiscale science mission profile and operations. *Space Sci. Rev.*, *199*, 77–103. (DOI:10.1007/s11214-014-0087-x)

Lapenta, G., Markidis, S., Divin, A., Goldman, M. V., & Newman, D. L. (2011). Bipolar electric field signatures of reconnection separatrices for a hydrogen plasma at realistic guide fields. *Geophys. Res. Lett.*, *38*, L17104. (DOI:10.1029/2011GL048572)

Lindqvist, P.-A., Olsson, G., & et al. (2016). The spin-plane double probe electric field instrument for mms. *Space Sci. Rev.*, *199*, 137–165. (DOI:10.1007/s11214-014-0116-9)

Matsumoto, H., Deng, X. H., Kojima, H., & Anderson, R. R. (2003). Observation of electrostatic solitary waves associated with reconnection on the dayside magnetopause boundary. *Geophys. Res. Lett.*, *30*, 1326. (DOI:10.1029/2002GL016319)

Phan, T. D., Eastwood, J. P., Cassak, P. A., Øieroset, M., Gosling, J. T., Gershman, D. J., & et al. (2016). MMS observations of electron-scale filamentary currents in the reconnection exhaust and near the X line. *Geophysical Research Letters*, *43*, 6060–6069. (DOI:10.1002/2016GL069212)

Pollock, C., Moore, T., Jacques, A., Burch, J., Gliese, U., Saito, Y., & et al. (2016). Fast plasma investigation for magnetospheric multiscale. *Space Sci. Rev.*, *199*, 331–406. (DOI:10.1007/s11214-016-0245-4)

Pritchett, P. L., & Mozer, F. S. (2009). Asymmetric magnetic reconnection in the presence of a guide field. *J. Geophys. Res*, *114*, A11210. (DOI:10.1029/2009JA014343)

Russell, C. T., Anderson, B. J., Baumjohann, W., Bromund, K. R., Dearborn, D., Fischer, D., & et al. (2016). The magnetospheric multiscale magnetometers. *Space Sci. Rev.*, *199*, 189–256. (DOI:10.1007/s11214-014-0057-3)

Swisdak, M., Drake, J. F., Price, L., Burch, J. L., Cassak, P. A., & Phan, T.-D. (2018). Localized and intense energy conversion in the diffusion region of asymmetric magnetic reconnection. *Geophys. Res. Lett.*, *45*, 5260–5267. (DOI:10.1029/2017GL076862)

Torbert, R. B., Russell, C. T., & et al. (2016). The fields instrument suite on mms: Scientific objectives, measurements, and data products. *Space Sci. Rev.*, *199*. (DOI:10.1007/s11214-014-0109-8)